

1 **Comparison of aerosol optical depth from satellite (MODIS),**
2 **sun photometer and broadband pyrhelimeter ground-based**
3 **observations in Cuba.**

4
5 Juan Carlos Antuña-Marrero¹, Victoria Cachorro Revilla², Frank García Parrado¹, Ángel de
6 Frutos Baraja², Albeth Rodríguez Vega¹, David Mateos², René Estevan Arredondo^{3,1}, Carlos
7 Toledano²

8
9 ¹ Atmospheric Optics Group of Camagüey (GOAC), Meteorological Institute of Cuba, Camagüey, Cuba

10 ² Atmospheric Optics Group (GOA), University of Valladolid (UVA), Valladolid, Spain

11 ³ Huancayo Observatory, Geophysical Institute of Peru, Huancayo, Peru

12
13
14
15
16
17
18 Resubmitted to *Atmospheric Measurement Techniques*

19
20 February 2018

21
22
23
24
25 Corresponding author:

26 Juan Carlos Antuña-Marrero

27 Atmospheric Optics Group of Camagüey

28 Meteorological Institute of Cuba

29 Camagüey, Cuba

30 Email: jcam45@gmail.com

33 **Abstract**

34 In the present study, we report the first comparison between the aerosol optical depth
35 (AOD) and Angstrom exponent (AE) of the MODerate resolution Imaging Spectroradiometer
36 (MODIS) instruments on the Terra(AOD_t) and Aqua(AOD_a) satellites and those measured using a
37 sun photometer at Camagüey, Cuba, for the period 2008 to 2014. The comparison of spatially and
38 temporally coincident Terra and Aqua data includes AOD derived with both Deep Blue (DB) and
39 Dark Target (DT) algorithms from MODIS Collection 6. Combined Terra and Aqua (AOD_{ta}) data
40 were also considered. Assuming an interval of ± 30 minutes around the time-overpass and the area
41 of 25 km around the site of the sun photometer, two collocated coincident criteria were taken:
42 individual pairs of observations and both spatial and temporal mean values, the latter of which we
43 call collocated daily means. The usual statistics (BIAS, MAE, RMSE) together with linear
44 regression analysis are used for this comparison. Results show very similar values for the two
45 criteria. For collocated daily means, the DT algorithm generally displays similar behavior for
46 AOD_t, AOD_a, AOD_{ta} compared to AOD_{SP} with lower values for the statistics and higher
47 homogeneity than the DB algorithm. Root mean square errors (RMSE) of 0.060 and 0.062 were
48 obtained for Terra and Aqua daily means with the DT algorithm, and 0.084 and 0.065 for the DB
49 algorithm, respectively. MAE follows the same patterns. Although BIAS for both Terra and Aqua
50 daily means presents positive and negative values, those of the DT algorithm are lower than the
51 DB algorithm. Combined AOD_{ta} data also give lower values of these three statistical indicators for
52 the DT algorithm. Both algorithms present good correlations for comparing AOD_t, AOD_a, and
53 AOD_{ta} with AODSP. In general, linear correlations for both algorithms are good, although the DT
54 algorithm yields better figures, giving slopes of 0.96 for Terra, 0.96 for Aqua and 0.96 for
55 Terra+Aqua compared to the DB algorithm which has slope values of 1.07, 0.9, 0.99, thus

56 displaying greater variability. Comparison with the AE showed similar results to those reported in
57 the literature concerning the two algorithms' capacity for retrieval. A comparison between
58 broadband AOD (BAOD) from broadband pyrhelimeter observations at the Camaguey site and
59 three other meteorological stations in Cuba and AOD observations from MODIS on board Terra
60 and Aqua show a poor correlation with slopes below 0.3, with the exception of Terra (0.38) for
61 both algorithms. Aqua(Terra) showed RMSE values of 0.073(0.080) and 0.088(0.087) for the DB
62 and DT algorithms. As expected, RMSE values are higher than those from the MODIS/sun
63 photometer comparison, although they are in the same order of magnitude. Results from the
64 BAOD, derived from solar radiation measurements, demonstrate its reliability to describe AOD
65 climatology at sites with no sun photometer and to produce historical AOD series estimates.

66

67 KEY WORDS: atmosphere, remote sensing, aerosols, Aerosol Optical Depth (AOD), Broadband
68 Aerosol optical depth (BAOD), AERONET, MODIS

69

70 **1. Introduction**

71 Atmospheric aerosols play an important role in weather and climate (IPPC 2013). Depending on
72 the physical/chemical and optical properties of atmospheric aerosols together with their origin and
73 spatial and temporal distribution, they can affect the Earth's radiative budget, as well as dynamic,
74 biogeochemical and chemical processes (Knippertz and Stuut, 2014; Seinfeld and Pandis, 2016).
75 All of these processes play a key role at a global and regional scale due to the high spatio-temporal
76 variability of aerosol properties. Aerosols can also affect the biosphere and, in particular, humans
77 in several ways: for example, the Saharan dust transported to America across the Atlantic supplies
78 nutrients to the Amazon forest (Swap et al., 1992; Yu et al., 2015). Moreover, in the Caribbean, in

79 addition to aerosols of local origin, dust makes the amount of aerosol exceed air quality standards
80 associated to human health (Prospero and Lamb, 2003; Prospero et al., 2014). The great variability
81 of Saharan dust transported to the Caribbean basin has been documented using long-term
82 observations in Barbados (Prospero and Lamb, 2003; Prospero and Mayol-Bracero, 2013) and
83 more recently in Miami, Guadeloupe and Cayenne (Prospero et al., 2014). The Caribbean region
84 is thus of great importance for aerosol studies due to its low aerosol background, which helps
85 aerosol transport studies (Kaufman et al., 2005; Denjean et al., 2016; Velasco et al., 2018). One
86 difficulty, however, is that it is an area where land and water make up a mixed pixel when remote
87 satellite aerosol studies are carried out.

88 In order to improve calculations of aerosol climatology for Cuban land areas, which
89 remains ongoing, we compared aerosol ground-based observations and available satellite data, as
90 a first step towards assessing this climatology. This involves a comparison between all the
91 available Camagüey sun photometer aerosol optical depth (AOD) data and the BAOD provided
92 by solar radiation measurements with the series of AOD (550 nm) from the MODerate resolution
93 Imaging Spectroradiometer (MODIS) instruments on board the Terra (2001 to 2015) and Aqua
94 (2002 to 2015) satellites. Selected observations were those spatially and temporally collocated
95 between satellite instruments and ground-based sites. In addition to the aerosol load given by the
96 AOD, we also evaluated the Ångström exponent (AE) as a parameter providing information about
97 particle size for MODIS and sun photometer data.

98 One of the challenges we faced was the low amount of potential coincident AOD and AE
99 from MODIS and the Sun photometer. The same is true for AOD from MODIS and broadband
100 pyrhelimeter derived BAOD, in both cases due to existing gaps in the ground-based time series
101 and also because this area is strongly affected by clouds (mainly partially cloud cover). In order to

102 maximize the number of satellite and surface measurement pairs, we used primary AOD and AE
103 L2 products without any averaging as well as combined AOD and AE from Terra and Aqua
104 MODIS sensors as a whole dataset. We also used Deep Blue (DB) and Dark Target (DT)
105 algorithms to evaluate the reliability of satellite AOD and AE retrievals to select the most
106 appropriate data set to derive the climatology of both AOD/AE aerosol parameters in Cuba.

107 The earliest attempt to measure aerosol optical properties at ground level in Cuba recorded
108 in a scientific publication dates back to 1988 (Martinez, 1988) where the Linke turbidity factor
109 and the Ångström β turbidity coefficient were derived from solar direct normal irradiance (DNI)
110 measurements. Twenty years later, a cooperation agreement between scientific institutions in
111 Spain and Cuba enabled a Cimel CE-318 sun photometer to be installed at Camagüey (Cuba) and
112 for it to be included in the Aerosol Robotic Network (AERONET, Holben et al., 1998). Several
113 aerosol studies have been conducted using the Aerosol Optical Depth (AOD) and AE from
114 Camagüey's sun photometer observations (see, Antuña-Marrero et al., 2016;
115 <http://www.goac.cu/uva/>).

116 Broadband pyrheliometric DNI observations allow the Broadband Aerosol Optical Depth
117 (BAOD) to be determined, which complements sun photometer aerosol observations at Camagüey,
118 and provides aerosol information at three other locations in Cuba. The main purpose of
119 determining BAOD is to offer information concerning aerosol variability over the island, also
120 making it possible to extend aerosol records back in time. The first BAOD calculations used for
121 DNI measurement were conducted at Camagüey under clear sky conditions for the period 1985-
122 2007 using Gueymard's (1998) improved parameterizations (Fonte and Antuña, 2011). García et
123 al. (2015) used this kind of DNI observation for a longer period (1981-2013) and compared this
124 BAOD to sun-photometer AOD data. They used observations under the clear line of sight between

125 the broadband pyrheliometer and a region of 5° around the Sun, as well as improved climatological
126 values of the integrated water vapor.

127 This comparative analysis does not aim to be a validation study of the MODIS sensor since
128 many works during the long history of the MODIS sensor on the Terra and Aqua platforms have
129 sought to improve its features (these include: Kaufman et al., 1997a, b; Tanré et al., 1997; Remer
130 et al., 2002, 2005, 2006; Hsu, et al., 2004,2006, 2013; Levy et al., 2007; 2009; 2010, 2013, 2015;
131 Sayer et al., 2013, 2014; <https://darktarget.gsfc.nasa.gov/atbd/overview>). However, compared to
132 other areas of the world, no studies have been reported in the Caribbean region and in Cuba in
133 particular (Papadimas et al., 2009; Mishchenko, et al., 2010; Kahn et al., 2011; Bennouna et al.,
134 2011, 2013; Witte et al., 2011; Gkikas et al., 2013; 2015; Levy et al., 2015).

135 As mentioned, our aim is to establish reliable aerosol climatology in Cuba based on satellite
136 and ground-based instruments. By making a detailed comparison of similarities and differences
137 between available data sets, the present work seeks to make a contribution to said aim.

138 The article is structured as follows. Section 2 begins with the description of the datasets,
139 followed by the explanation of the coincidence criteria between the AOD and AE MODIS L2
140 products and the same two variables from the sun photometer and broadband pyrheliometer
141 BAOD. This section ends with the explanation of the statistical indices used. Section 3 is composed
142 of various sections designed to explain and discuss the large volume of results to emerge from the
143 comparison given by taking two different retrieval AOD aerosol algorithms, for both the Terra and
144 Aqua platforms, with the sun photometer and BAOD. Section 4 contains a summary of the
145 conclusions.

146

147 **2. Materials and Methods**

148 **2.1 MODIS satellite instruments**

149 The twin MODIS instruments on board the Terra and Aqua satellites have accumulated
150 over 15 years of observations of several atmospheric parameters, including AOD at several
151 wavelengths and the AE parameter, the two most common parameters for describing atmospheric
152 aerosol optical properties. Based on the assumptions about the properties of the Earth’s surface
153 and the aerosol type expected over these surfaces, the MODIS Atmosphere team developed three
154 algorithms for processing MODIS observations (Levy et al., 2013). Regions which appear visually
155 “dark” from space, referred to as Dark Target (DT), include the algorithm assumptions for
156 vegetated land surfaces (Kaufman et al., 1997a, b) and for remote ocean regions (Tanré et al.,
157 1997). The third algorithm, called the Deep Blue (DB) algorithm, includes assumptions for
158 surfaces which are visually “bright” from space and uses near-UV wavelengths (DB band near 410
159 nm). Under these conditions, the DB band provides a better signal than the visible wavelengths,
160 improving the information content for aerosol retrievals (Hsu et al., 2004; 2006) due to lower
161 surface albedo at this short wavelength. Levy et al. (2013) provide a detailed explanation of basic
162 MODIS retrieval concepts and improvements to the DT algorithm in Collection 6 for aerosol
163 products. In addition, Hsu et al. (2013) give a detailed explanation of the DB algorithm
164 improvements in Collection 6.

165 Following Levy et al. (2013), we summarize the MODIS calculus chain. MODIS Level 0
166 (L0) is the basic data file containing raw observations from the sensors. Observations grouped in
167 five-minute swath scans (called granules) are Level 1A (L1A), which after calibration becomes
168 Level 1B (L1B). L1B data feed the MODIS geophysical retrieval algorithms, generating the
169 primary geophysical observations, which include AOD and AE, designated Level 2 (L2). This is
170 followed by Level 3 (L3), consisting of daily and monthly statistics of geophysical products, in 1°

171 x 1° latitude\longitude grid boxes. L2 aerosol products are stored in the MOD04 (Terra) and
172 MYD04 (Aqua) files.

173 We selected AOD at 550 nm from MODIS (both on Terra and Aqua satellites) Collection
174 6, L2 data level derived using the two algorithms; DB for land with the highest data quality
175 (Quality flag = 2, 3) and DT for land, corrected (Quality flag = 3). In addition, we selected the AE
176 retrieved over land from the DB algorithm using the corresponding pairs of AOD values (412/470
177 nm or 470/650 nm) with the highest quality (Quality flag = 2, 3), since the DT algorithm only
178 retrieves the AE over the ocean (Table B1 in Levy et al., 2013). Table 1 lists the aerosol products
179 used in the present study.

180 At a global scale, it has been established that using the DT algorithm over land, MODIS-
181 retrieved aerosol size parameters evidence poor quantitative capacity, particularly AE (e.g., Levy
182 et al., 2010; Mielonen et al., 2011). However, for the DB algorithm, AE capacity increases for
183 moderate or high aerosol loadings, $AOD > 0.3$ (Sayer et al., 2013). We therefore decided to
184 conduct the comparison between the AE from the MODIS DB algorithm and the AE from the
185 Camagüey sun photometer to estimate its uncertainty. The enhanced DB algorithm methodology
186 for deriving AE in Collection 6 is the same as in Collection 5. It uses the Ångström power law and
187 AOD values at 412, 470 and 650 nm. Under non-vegetated surfaces, AE is derived using the AOD
188 from pair 412/470 nm. For vegetated surfaces, AE is derived from the 470/650 nm pair. In the case
189 of a surface with mixed vegetated and non-vegetated areas, AE is derived using the AOD at the
190 three wavelengths mentioned (Hsu et al., 2013).

191

192

193 ***2.2 Camagüey AERONET sun-photometer***

194 The Camagüey sun photometer, installed thanks to an agreement between the University
195 of Valladolid (UVA), Spain, and the Meteorological Institute of Cuba (INSMET) for joint aerosol
196 research, contributes to the NASA Aerosol Robotic Network (AERONET) (Antuña et al., 2012).
197 Annual replacement of the instrument for one calibrated, sent from Valladolid to Camagüey,
198 encountered numerous transportation and customs delays, causing gaps in the observation series.
199 However, the collected series of observations does represent a valuable dataset of aerosol columnar
200 optical properties in the Caribbean, enabling GOAC-INSMET and GOA-UVA to conduct
201 preliminary aerosol research (Antuña-Marrero et al, 2016).

202 The AERONET Cimel sun photometers have been conducting aerosol observations at nine
203 spectral narrow band filters for over two decades, producing spectral AOD and column effective
204 particle properties (Holben et al., 1998). In general, Cimel sun photometer nominal wavelengths
205 are 340, 380, 440, 500, 675, 870, 935, 1020 and 1640 nm. In some cases, the 1640 nm is replaced
206 by a 1240 nm. Its processing algorithm, based on the Beer-Lambert-Bouguer law, allows spectral
207 OD values at an uncertainty level of approximately 0.01 to 0.02 to be determined (Holben et al.,
208 1998; Eck et al., 1999). Because of this low level of uncertainty, AERONET AOD observations
209 commonly serve as reference values (“ground truth”) to validate AOD measured by other remote
210 sensing sensors (Zhao et al., 2002). AERONET AE are derived for five different wavelength
211 intervals; 340-440 nm, 380-500 nm, 440-675 nm, 440-870 nm and 500-870 nm. In the present
212 study, the selected AE is the one in the 440-675 nm range (AE_{SP}).

213 We used Camagüey sun photometer Level 2.0 data as processed by AERONET, i.e., cloud
214 screened and quality-assured (Smirnov et al., 2000), covering the period from 7 October 2008 to
215 1 August 2014. This consisted of 29,940 single AOD (340 to 1640nm) and AE_{SP} observations.

216 Applying the Ångström power law, we converted single sun photometer AOD observations at 500
217 nm wavelength to AOD at 550nm, (AOD_{SP}) using the AE_{SP} from the same measurement:

218

$$AOD_{SP} = AOD_{500} \left(\frac{\lambda_{550}}{\lambda_{500}} \right)^{-AE_{SP}} \quad (1)$$

219

220 ***2.3 Solar direct irradiance measurements and derived Broadband Aerosol Optical*** 221 ***Depth(BAOD)***

222 Four actinometrical stations belonging to the “Diagnostic Service for Solar Radiation in Cuba”
223 provided the DNI observations used to derive the BAOD (Antuña et al., 2008; 2011). Table 2 lists
224 the WMO code of the four stations, the geographical location and the number of observations
225 available for the periods at each station. Figure 1 shows the geographical location of the four
226 stations. The stations are equipped with Yanishevsky manual broadband solar radiation
227 instruments supplied between the 1970s and 1980s by the Hydrometeorological Service of the
228 Soviet Union. The Yanishevski broadband pyrheliometer is the M-3 model, a thermo-battery
229 system with a 5° field of view connected to an analogic galvanometer, GSA-1MA or GSA-1MB
230 model (GGO, 1957).

231 Calibrations of all the actinometrical instruments are conducted periodically by comparison
232 with a master broadband pyrheliometer and a master pyranometer. Trained observers perform
233 hourly manual observations from sunset to sunrise, following the standard methodologies and
234 quality control procedures established for this set of instruments (GGO, 1957). Once manual
235 measurement is conducted and recorded in a notebook designed for the purpose, all the
236 measurement information is digitized using Actino version 2.0 software (Estevan, 2010; Antuña
237 et al., 2008) of the “Diagnostic Service of the Broadband Aerosol & Clouds Optical Depth for

238 Cuba” (<http://www.goac.cu/eoc/>), a public service provided by GOAC. The software includes a
239 robust quality control of input data, its processing and output quality control (Antuña et al., 2011).
240 Because of the ageing of the Soviet era instruments, the magnitude of the error associated to the
241 broadband pyrheliometers currently operating in Cuba is estimated to be around 10 %.

242 Based on the model parameterization of solar broadband irradiances, the integrated aerosol
243 optical depth δ_a , BAOD, can be obtained using equation (2), where direct normal solar irradiance
244 (DNI) is measured and the remaining variables are determined independently (Gueymard, 1998).

245

$$246 \quad \delta_a = \left(\frac{1}{m_a} \right) \left[\ln \left(\frac{E_{0n}}{DNI} \right) - m_R \delta_c - m_w \delta_w - m_{nt} \delta_{nt} \right] \quad (2)$$

247 The individual atmospheric processes considered are: Rayleigh scattering, absorption by
248 ozone (O₃), stratospheric and tropospheric nitrogen dioxide (NO₂), uniformly mixed gases, water
249 vapor, and extinction (mostly scattering) by aerosols. The variables in equation (2) are: optical air
250 mass of aerosols (m_a), Rayleigh scattering, uniformed mixed gases, O₃ absorption and
251 stratospheric NO₂ (m_R), water vapor (m_w) and tropospheric NO₂ (m_{nt}) and similarly the
252 corresponding broadband optical depths δ . The method makes a series of assumptions, i.e.,
253 Bouguer’s law; in the strict sense that it is only valid for monochromatic radiation and is applied
254 to define broadband transmittance. For a detailed description of the derivation of equation (2) and
255 the parameterization of the variables, see Gueymard, (1998), and Fonte and Antuña (2012) and
256 García et al. (2015) for the method’s application to our data.

257 In order to avoid cloud contamination in BAOD retrieval, we used only DNI observations
258 with the cloud-free condition in the line of sight to the sun, in other words with a clear line of sight
259 between the broadband pyrheliometer and a region of 5° around the sun (GOAC, 2010).
260 Furthermore, to avoid errors associated with high elevation zenith angles, causing larger air

261 masses, DNI observations performed at 6:00 and 18:00 Local Time (LT) were not used in the
262 present study.

263 The main errors of the method for determining BAOD are associated to instrumental errors
264 and the error when estimating the precipitable water (PW) component (Gueymard, 2013). In the
265 first case, in order to ensure the quality of the solar radiation dataset from the four actinometrical
266 stations used in this study, including DNI, they are regularly subject to a two-step quality control
267 (Estevan et al., 2012). The first step applies the standard procedures designed for Yanishevski type
268 actinometrical instruments from the former Soviet Hydro-Meteorological Service (Kirilov et al.,
269 1957). Data that pass this quality procedure are then evaluated following the standards set by the
270 Baseline Solar Radiation Network - BSRN (Ohmura 1998, Long and Shi, 2006; 2008; Estevan et
271 al., 2012).

272 The size of the field of view of the broadband pyrhemometers is another potential source
273 of error since, in certain cases, circumsolar radiation causes more radiation to be measured than
274 expected. In such cases, the effect is an underestimation of BAOD. Nevertheless, this effect is low
275 in general, except in specific conditions such as large air masses, in the presence of high aerosol
276 loads or of large-particle aerosols (Gueymard, 1998).

277 Monthly mean PW values at the four actinometrical stations were used as input to derive
278 monthly mean δ_w values (Gueymard, 1998). For Camagüey, we calculated the monthly mean PW
279 values from the sun photometer PW observations from 2008 to 2014 (García et al., 2015). For
280 each of the three other stations, we calculated the monthly mean PW values using the vertical
281 integrated water vapor (kg m^{-2}) from spatially coincident ERA-Interim reanalysis between 1979
282 and 2013 (Barja et al., 2015). Taking into account all the above-mentioned errors, the total
283 uncertainty of the method used to determine BAOD is in the order of 10^{-2} (Gueymard, 1998).

284 **2.4 Coincidence criteria for MODIS and Sun photometer observations**

285 Obtaining sufficient AOD satellite observations over land for climatological studies in
286 insular areas poses a challenge when compared to the amount of data usually available over
287 continental regions such as the US, Europe or China. The reason tends to be the small size of the
288 islands. In the case of Cuba, its particular narrow latitudinal and elongated longitudinal extension
289 combined with its irregular coasts renders the MODIS L3 product unsuitable for climatological
290 studies. As can be seen in Figure 1, most of the 1° by 1° grid cells consist of both land and sea
291 areas, resulting from the merging AOD measured over the two surfaces. The red grid cell in Figure
292 1 is an example of the limitations of MODIS L3 products to represent land areas in the case of
293 Cuba. In response to this, we plan to use the MODIS L2 product to produce aerosol climatology
294 for Cuba rather than L3, which is commonly used for this type of studies. In this regard, it is vital
295 to validate the single observations from MODIS L2 with the single sun photometer observations.
296 We designed and applied a method to maximize the available pairs of MODIS L2 and sun
297 photometer AOD and AE observations coincident in space and time, avoiding duplicating the use
298 of any of them. Additionally, in an effort to increase the amount of data, we tested the differences
299 between Terra and Aqua L2 MODIS AOD and AE observations in order to determine the possible
300 combination of both Terra and Aqua in a single dataset.

301 Hereinafter, AOD_t , AOD_a , AOD_{ta} and AOD_{SP} will denote spatio-temporal AOD from
302 collocated MODIS (Terra, Aqua and Terra + Aqua) and AERONET sun photometer data,
303 respectively. Unless otherwise indicated, “AOD” refers to AOD at 550 nm wavelength. Similarly,
304 AE from Terra, Aqua and Terra + Aqua derived using only the DB algorithm will be denoted as
305 AE_t , AE_a and AE_{ta} .

306 Given the challenges arising from the small amount of potential coincident spatial and
307 temporal AOD_t and AOD_a with AOD_{SP} and BAOD, as explained above, we used MODIS L2 data
308 to maximize the amount of available MODIS observations for comparison. Hereinafter, we call
309 these observations “single observation values”; using the same denomination for the instantaneous
310 sun photometer observations on each day and for hourly broadband pyrhelimeter observations.
311 Another way to increase the amount of data was to combine AOD_t and AOD_a (AOD_{ta}) for
312 comparison with AOD_{SP} and BAOD. In these cases, different observations of AOD_{SP} and BAOD
313 match AOD_t and AOD_a because the time difference established for coincidence (± 30 min) is lower
314 than the difference between the Terra and Aqua daily overpass times.

315 Spatial coincidence criteria were guaranteed by selecting all the AOD_t and AOD_a measured
316 inside the 25 km radius around the sun photometer site for the whole data period from each satellite
317 sensor. Table 3 shows the amount of spatial coincident information for non-negative AOD_t and
318 AOD_a values. It shows the amount of data available for the whole period 2001 to 2015, when
319 broadband pyrhelimeter observations at Camagüey are available, and 2008 to 2014, the period of
320 available sun photometer observations. There are at least twice as many available observations
321 from Terra as from Aqua for the two periods. The greater number of available data from Terra
322 compared to Aqua is associated to the different overpass times of the two satellites over Cuba.
323 Figure 2 shows that Terra overpasses occur in the mid to late morning before convective activity
324 begins, while the Aqua overpasses take place in the early afternoon when convection has already
325 begun, causing a higher number of observations to be discarded in AOD retrievals due to cloud
326 presence.

327 **2.4.1 Collocated “*Single observation*” values and “*daily mean*” values**

328 All Aqua and Terra overpass times in a radius of 25 km around Camagüey for the periods
329 2001 to 2015 (Terra) and 2002 to 2015 (Aqua) are shown in Figure 2. Overpass times, defined by
330 the maximum and minimum values of all the 25 km spatially coincident MODIS observations, are
331 10:12 – 11:49 (LT) for Terra and 12:47 – 14:20 (LT) for Aqua. In addition, Figure 2 shows the
332 diurnal frequency of sun photometer observations from 2008 to 2014, and the diurnal frequency
333 of the BAOD observations for Camagüey for the period 1981 to 2015. Note that the BAOD
334 histogram shows only hourly frequency values, since that is the time interval between the manual
335 pyr heliometric observations.

336 For each day, we compared the corresponding time of each single sun photometer
337 measurement with the time of each single AOD_t and AOD_a observation located in a radius of 25
338 km around the sun photometer site (an area of almost 2,000 km²) and in the time window of ± 30
339 minutes between both types of observations. The former selection process includes, for each
340 satellite, the AOD_t and AOD_a values derived both with the DB and DT processing algorithms
341 separately, producing four independent bulk datasets, two for Aqua and two for Terra. We then
342 identified four different cases of matching data per day in the bulk coincident datasets. The first
343 consisted of days with only one AOD_{SP} value and one AOD_t (AOD_a) coincident value, and the
344 second, only one AOD_{SP} value coincident with multiple AOD_t (AOD_a) values each day. In the
345 third case, only one AOD_t (AOD_a) value coincided with multiple AOD_{SP} values. Finally, the fourth
346 case consisted of multiple AOD_{SP} values coincident with multiple AOD_t (AOD_a) values.

347 Coincident cases were then selected for comparison, case by case. In the first instance, we
348 selected all cases. In the second case, because of the MODIS instruments spatiotemporal sampling
349 geometry, time differences between MODIS and sun photometer observations are in the order of
350 one minute. As a result, only the criterion of the minimum distance between the positions of the

351 AOD_t (AOD_a) and the sun photometer was applied to determine the pair of coincident values,
352 therefore not allowing any repeated AOD_{SP} and AOD_t (AOD_a) values to be selected. Since it
353 consists of only one AOD_t (AOD_a) measurement and multiple AOD_{SP} observations, in the third
354 case the distance is the same; hence the selection criteria was the minimum of the time differences
355 between AOD_{SP} and AOD_t (AOD_a) observations. The fourth case, the most complicated, allowed
356 both criteria to be applied; the minimum in distance and time. No differences in the amount of
357 coincident data were found when testing whether the order in which the two criteria were applied
358 had any impact.

359 Another approach, the most commonly used for comparison (Bennouna et al., 2011; Sayer
360 et al., 2014), involves the average of all the AOD_{SP} values in the interval of ± 30 minutes compared
361 to MODIS instrument overpass time (note that AOD_t and AOD_a averages are really the daily values
362 of MODIS) located in a radius of 25 km around the sun photometer. At least two single AOD_{SP}
363 and two single AOD_t (AOD_a) observations were required to calculate the spatio-temporal average.
364 We applied a similar approach to calculate collocated daily means AE_{SP}, AE_t and AE_a. The
365 procedures described above generated a series of collocated daily means of AOD_{SP} versus AOD_t
366 (AOD_a) and AE_{SP} vs. AE_t (AE_a). Hence, by combining the former generated series of AOD (AE)
367 for Terra and Aqua we produced the coincident (Terra + Aqua) dataset. The term *collocated daily*
368 *mean AOD* will be used hereinafter although it should be stressed that this approach reduces the
369 number of observations generated by virtually a third.

370 After explaining the coincidence criteria adopted here, it is well known that this type of
371 comparison shows major differences depending on the spatial and or temporal resolution taken for
372 the MODIS sensor in relation to the ground-based instruments used (Santese et al., 2007; Levy et
373 al., 2009; Bennouna et al., 2011, 2013). The justification for using a “single observations” dataset

374 and a “collocated daily means” dataset separately to analyze this comparison is based on: a) the
375 characteristics of the surface area under study, with nearby areas of water and land; b) the
376 difference concerning how cloud cover affects data during the overpass time of the Terra and Aqua
377 platforms; and c) the possibility of including the largest amount of data; d) the fact that only single
378 observations can be compared in the case of BAOD pyrheliometer measurements.

379 **2.5 Statistics**

380 The statistics used in the present study are those commonly used (e.g., Sayer et al., 2014).
381 These are the root mean square error (RMSE), mean absolute error (MAE), median bias (BIAS),
382 the Pearson linear correlation coefficient (R), the number of coincident MODIS and sun
383 photometer cases (Cases) and the fraction (f) of the MODIS/AERONET AOD retrievals in
384 agreement within the expected uncertainty. Expected uncertainty, defined as a one standard
385 deviation confidence interval entails the sum of the absolute and relative AOD errors. Usually
386 referred to as “expected error, EE”, it was applied in accordance with equation 3 (Sayer et al.,
387 2014)

$$388 \quad EE_{DT} = \pm(0.05 + 0.15 AOD) \quad (3)$$

389 The aim is to compare the performance of the DB and DT algorithms directly (Sayer et al.,
390 2014). All of these statistical indicators were evaluated for the whole set of collocated AOD_t,
391 AOD_a, AOD_{ta} with AOD_{SP}, and BAOD; AE_t, AE_a, AE_{ta} with AE_{SP}; as well as time frequencies
392 (Figure 2) and histograms of these quantities. We also evaluated these statistics on a monthly scale
393 for the AOD values.

394

395 **3. Results and Discussion.**

396 This section is divided into four subsections. In the first subsection, we analyze in detail
397 the main results from comparing the AOD satellite MODIS sensors and the sun photometer data
398 given by the statistical indicators and linear correlations, as a result of taking two different criteria,
399 two different retrieval AOD aerosol algorithms both for the Terra and Aqua platforms. Section 3.2
400 analyzes the same type of results but under the perspective of monthly values since they represent
401 the climatology of AOD and the associated uncertainties. Section 3.3 shows AE behavior and
402 Section 3.4 analyzes the comparison of satellite MODIS data in relation to broadband aerosol
403 optical depth from solar radiation.

404 **3.1 Comparison of AOD retrievals from sun photometer and MODIS satellite instruments.**

405 As explained, we selected MODIS AOD_t (AOD_a) and sun photometer AOD_{SP} data based
406 on two different criteria for their comparison. Results are shown in Tables 4 and 5, corresponding
407 to collocated daily means and single observations, respectively. The values of all the statistics of
408 these two tables are extraordinarily similar, with analogous behavior for the different algorithm
409 and platforms. In truth, no substantial differences are found. It must be noted that Table 4 for
410 collocated daily means contains a third less data than Table 5 based on single observations. In
411 contrast, however, the latter data have a higher associated error than daily mean data. This result
412 cannot be foreseen a priori but clearly demonstrates that either criterion may be taken, since the
413 result is basically the same.

414 Taking Table 5 together with Figure 3 of collocated daily mean values, we then analyze
415 the different behavior of the two algorithms for the Terra and Aqua platforms, when AOD_t (AOD_a)
416 from satellite are compared with the sun photometer, AOD_{SP} . Figure 3 shows the density plots of
417 the collocated daily mean AOD values from the sun photometer versus those of MODIS
418 instruments for Terra, Aqua and combined, for DB (top plots) and DT (bottom plots) algorithms.

419 The least squares linear fit lines and equations are also shown in the figure while the correlation
420 coefficients (R values) are in Table 5. In general, the plots show that low loading aerosols
421 predominate and that scatter increases for higher aerosol loadings, with a slight overestimation of
422 AOD_t (AOD_a) satellite data compared to AOD_{SP} . In all cases, the slopes are between 1 and 0.9 and
423 the intercepts are in the order of 10^{-2} (with lower values for the DT algorithm), showing very good
424 values of these parameters for Terra and Aqua for both the DT and DB algorithms.

425 Figure 3 shows that the DT algorithm displays generally better behavior than the DB
426 algorithm. The DT algorithm evidences more unified behavior as can be seen for the slope values
427 (0.96 for both Aqua and Terra) while DB changes, giving a value above 1 (1.069) for Terra and
428 below 1 for Aqua (0.901). However, these differences are not very relevant since both algorithms
429 give almost identical R values, and the difference appears for the platforms, with higher values for
430 Aqua than for Terra (~0.78 and ~0.73, respectively). A compensation effect can be observed when
431 data are combined, since in this case the slope of the DB algorithm is closer to 1 than the DT
432 algorithm, although the intercept is higher (closer to 0 for DT algorithm). For combined data, the
433 two algorithms show a more similar behavior than for separate Aqua or Terra results. Analyzing
434 Table 5, the magnitudes of the RMSE, MAE, BIAS and f statistics are lower for the DT than for
435 the DB algorithm (see the higher values of DB for Terra, column 1, and the more similar values in
436 the other columns). As mentioned, the values of these four parameters show that the DT algorithm
437 presents a more unified behavior for both platforms than the DB, which has similar values for
438 Aqua but which change significantly for Terra.

439 Although the statistical numbers in the comparison depend on the area under study,
440 comparisons between areas are always possible. A recent validation of MODIS Collection 6 AOD_a
441 (Aqua), derived using the DB algorithm, with AOD_{SP} from six AERONET stations in

442 Central/South America (CSA) and seven in Eastern North America (ENA) was reported by Sayer
443 et al. (2013). The number of pairs of collocated MODIS and AERONET daily averaged
444 observations for CSA (ENA) was 3,032 (4155). Sun photometer data were averaged within the 30
445 minute MODIS overpass time and MODIS data were averaged in the 25 km radius around the sun
446 photometer site, which makes the comparison appropriate. We selected the BIAS and R statistics
447 in Table 1, which were defined as in the present study (Sayer et al., 2013).

448 We compare those statistics with the ones given in Tables 4 and 5, calculated for
449 Camagüey. The BIAS for the CSA (ENA) stations is -0.016 (0.0094), although those of Camagüey
450 for both single observations and collocated daily means are (-0.027 and -0.033), thus showing
451 higher values for Camagüey and similar signs for CSA and the opposite for ENA. R values for
452 Camagüey for single observations and collocated daily means are 0.82 and 0.79, respectively,
453 lower by around 10 % (5 %) than the R values of 0.96 (0.86) for the CSA (ENA). However, it
454 should be noted that the number of cases used for the statistics at Camagüey was 419 for single
455 observation and 169 for collocated daily means, representing 6 % and 14 % of the 3,032 cases
456 used in the cited study. In addition, none of the stations in the CSA (ENA) regions were located in
457 the Caribbean, but south and north (Sayer, 2018). Despite the significant difference in the amount
458 of cases used in both studies and the location of the six stations, results show reasonable agreement.

459 *3.2 Monthly means values and statistics*

460 Given the close similarity in the results from single observations and collocated daily
461 means data, it seems reasonable to evaluate monthly mean values based on only one of them, i.e.,
462 for the collocated daily means data. Figure 4 shows the monthly means (based on the mean of each
463 month for every year of the measured period) and the statistics resulting from the comparison
464 between AOD_{SP} and AOD_{ta} for both the DB and DT algorithms. Tables S1 and S2 (see

465 supplementary material) also illustrate this comparison although they add separate information for
466 Terra and Aqua (see supplementary material). In Figure 4a, the multiannual monthly means from
467 the combined AOD_{ta} and AOD_{SP} for both the MODIS DB and DT algorithm are shown, providing
468 an initial overview of aerosol AOD climatology in Camaguey. It can also be seen that the DT
469 algorithm gives the best match with monthly mean AOD_{SP}.

470 The monthly RMSE and MAE plots in Figures 4b and 4c generally show increases, with
471 the increase in the AOD_{ta} for the DT algorithm and also for the DB algorithm, the exception being
472 the minimum in April for the DT algorithm (this means greater differences between satellite and
473 sunphotometer in summer than in winter). These results are consistent with the fact that AOD
474 uncertainty depends on the AOD itself (see eq. 3) and greater AOD variability in summer. The
475 AOD_{ta} peaks for the DT algorithm in March in both RMSE and MAE are also present in the results
476 for AOD_t and AOD_a, separately, and the amount of cases available for the statistics is among the
477 highest of all the months seen in Tables S1 and S2 (see supplementary material). In Table S2, for
478 the DT algorithm, we can see that the number of cases of AOD_{ta} from March to April drops by 55
479 %. However, something similar happens for the DB algorithm in Table S1, with the number of
480 AOD_{ta} cases falling from March to April by 61 %. Sampling cannot therefore be seen as the cause
481 of the RMSE and MAE peaks for the DT algorithm. We plan to revisit this feature in future studies.
482 In summer, RMSE and MAE show their maximum values associated to the maximum values of
483 the AOD resulting from Saharan dust reaching Cuba from across the Atlantic. The BIAS is
484 negative in summer for both Terra and Aqua AOD, showing that AOD_t and AOD_a observations
485 have higher magnitudes than AOD_{SP}.

486 Tabulated results of the comparison between AOD_t, AOD_a and AOD_{ta} with AOD_{SP} on a
487 monthly scale also show better results for the DB (see Table S1) than for the DT (Table S2)

488 algorithm. Here, we only discuss the results of the joint AOD_{ta} dataset using both the DT and DB
489 algorithms. In Figures 4d, the BIAS for the DT algorithm is positive from December to May, a
490 period of the year with predominant lower AOD_{ta} and AOD_{SP} values. During this period, AOD_{ta}
491 underestimates AOD_{SP}. BIAS then becomes negative from June to November, which is when
492 Saharan dust reaches the Caribbean basins. At the same time, the BIAS of the AOD_{ta} derived with
493 the DB algorithm is negative for the whole year, with higher absolute values than those from the
494 DT algorithm.

495 The correlation coefficient, R, in Figure 4e is the statistic which shows almost the same
496 agreement for the DB and DT algorithm. However, the DT shows a higher number of R-values
497 bearing higher magnitudes. R magnitudes remain over 0.5 almost the whole year round except in
498 December and January when lower AOD values occur.

499 Figure 4f shows the fraction of the AOD_{ta} (f), in agreement with AOD_{SP} within the expected
500 uncertainty, showing its higher values over 80 % from November to January, in general for both
501 algorithms. This is the period of the year with the lowest monthly mean values of both AOD_{ta} and
502 AOD_{SP}. During the rest of the year, including the period of the Saharan dust arrivals, it shows its
503 lowest values between 60 % and 75 % for the DT algorithm while values for DB below 50 % occur
504 in four of the months between June and October. The discontinuous blue line at f = 68 % denotes
505 a one standard deviation confidence interval, selected to describe EE. The f values above that value
506 mean the algorithm works better than expected. All the statistics demonstrate that the DT algorithm
507 performs better than the DB for the region of study. However, the lowest R values for those months
508 with the highest f values would seem to be contradictory. At present, we have no explanation for
509 this.

510 ***3.3 Comparison of Ångström Exponent by sun photometer and MODIS satellite instruments:***

511 Figure 5 shows the frequency distribution of the coincident AE_{SP} with both AE_t and AE_a
512 using the DB algorithm, as explained. As can be seen in the literature, the Ångström Exponent
513 varies between 0 and 2. Our Ångström Exponent data obtained from the AERONET sun
514 photometer measurements are within this range with a wide and smooth frequency distribution of
515 values and with a not well-defined maximum in the range 1.2 and 1.6. Neither AE_t nor AE_a present
516 any real distribution shape because there are practically no values below 1, with most being around
517 $AE = 1.5$, followed by a second maximum at $AE = 1.8$. The first, 1.5, is a regional default value
518 for AE_t and AE_a (Hsu et al., 2013; Sayer et al., 2013) assumed by the DB algorithm in the case of
519 low AOD values (AOD_t or $AOD_a < 0.2$). The second is associated with the fact that the AE_t and
520 AE_a values allowed by the aerosol optical models in Collection 6 are constrained between 0 and
521 1.8 to avoid unrealistic values (Sayer et al., 2013).

522 Table 6 shows the results of the comparison of coincident AE_t , AE_a and AE_{ta} with E_{SP} . For
523 both single observations and collocated daily mean data the statistics were calculated for the two
524 options: the first including all values and the second excluding cases with $AE = 1.5$ and 1.8. The
525 statistics in Table 6 for all values present similar values considering those derived by single
526 observation or for collocated daily mean values as expected once we know the results for AOD,
527 although similar values also appear for Terra and Aqua (no clear distinction appears between Terra
528 and Aqua). These statistics present very high values if compared with those shown for AOD.
529 Obviously, the R correlation coefficient presents very low values, which are below 0.5 (the poor
530 correlation is observed in the scatter plots similar to those in Figure 6, not shown here). Excluding
531 AE_t and AE_a values equal to 1.5 or 1.8 entails no substantial difference, only lower BIAS values.
532 Overall, the results of the comparison showed the low quantitative skill of the AE_t and AE_a for this
533 site. One factor contributing to this result is that the AE from the MODIS DB algorithm displays

534 great uncertainty for low-AOD conditions, since AE is obtained as a gradient between two small
535 AOD numbers (Wagner and Silva, 2008).

536 *3.4 Comparison of AOD between MODIS products and BAOD for the four Cuban* 537 *actinometrical stations.*

538 Two main facts limit the number of available BAOD values coincident in time with AOD_t
539 and AOD_a: the hourly time step between manual DNI observations and the required condition of
540 a clear line of sight between the pyrheliometer and a region of 5° around the Sun. Consequently,
541 only one BAOD measurement could coincide each day with AOD_t, and another with AOD_a given
542 the time coincidence criteria. Table 7 lists the number of coincident AOD_t, AOD_a, AOD_{ta}
543 observations in space and time with BAOD both for the DB and DT algorithms for each of the
544 actinometrical stations. Since the amount of coincident observations at each station is low, we
545 decided to combine all the pairs of AOD_t, AOD_a and AOD_{ta} coincident with BAOD in the four
546 sites together in order to conduct the comparison. In addition, we did not consider the very few
547 cases with values of BAOD > 0.6, around 1 % of all cases, so as to avoid the possibility of
548 inadvertent cloud contamination.

549 Table 8 contains almost the same statistics used in previous comparison satellite-sun
550 photometer data (see Table 4 and 5), both for the DB and for DT algorithms for the four
551 actinometrical stations together. The only statistic not included in Table 8 is f, the fraction of the
552 MODIS/AERONET AOD retrievals in agreement within the expected uncertainty, because such
553 uncertainty still has to be established for BAOD. We highlighted the best performing algorithm in
554 bold for each of the statistics. The AOD_a derived with the DB algorithm performs better than the
555 other three combinations of AOD_t, AOD_a, for DT and DB in accordance with all four statistics,
556 except for BIAS, where the best performing is still the DB algorithm, but for AOD_t. However, in

557 general and taking into account the low number of data and the fact that we have single
558 observations, the RMSE, MAE and BIAS for AOD_t, AOD_a, AOD_{ta} derived with both DB and DT
559 algorithms remain in the same order of magnitude as earlier Tables 4 and 5, with the exception of
560 the low values of the correlation coefficient R. The BIAS shows almost similar behavior except
561 for its best performing value. This different behavior of algorithms and platforms with respect to
562 the earlier results of Table 4-5 is clearly shown by Figure 6 where the scatter plots of the BAOD
563 vs. AOD_t, AOD_a, and AOD_{ta} are depicted. What is clear is the poor correlation given by the very
564 low values of the slope with respect to the value 1 and also the relatively high values of the intercept
565 in relation to 0, and hence the resulting low values of the R coefficient. BAOD shows a high
566 uncertainty for low values of AOD (below 2, see this range over the X axis in the plots) which are
567 those prevalent in this area (1).

568

569 **4. Conclusions**

570 This study addresses the comparisons of different sources of AOD and AE from ground-
571 based sun photometer (AERONET level 2.0 data), MODIS instruments (Terra, Aqua, and Terra +
572 Aqua) and retrievals from direct normal solar irradiance observations in Cuba. Although this type
573 of comparison shows important differences depending on the spatial and temporal resolution of
574 MODIS and ground-based instruments, justification for using a single observations dataset and
575 collocated daily means data set separately to analyze this comparison here is based on the
576 characteristics of the surface area under study, with nearby stretches of water and land. Another
577 reason is the difference with regard to how cloud cover at the overpass time of the Terra and Aqua
578 platforms affect the aerosols observations. Despite the different number of observations given by

579 the two selected criteria, the overall results shown by the statistics are very similar and show alike
580 patterns, which are therefore equal from the analysis perspective.

581 The results of the comparison between spatial and temporal coincident single observations
582 and collocated daily means of AOD_{SP} vs. AOD_t (AOD_a) show better performance for the Dark
583 Target (DT) algorithm. Furthermore, we found small differences between AOD_t and AOD_a , thus
584 justifying the combination of these observations in a single dataset, and thereby improving the
585 behavior of both algorithms. Evaluation of multiannual monthly means of collocated daily mean
586 AOD_{ta} reveals better agreement with AOD_{SP} for the DT algorithm and a clear overestimation for
587 the DT algorithm, corroborated by the statistics. Statistics show a direct relation between the
588 RMSE and MAE values and the monthly mean values of AOD_{ta} . The BIAS and fraction of data
589 within the uncertainty margins (f) show an inverse relation with the monthly mean values of
590 AOD_{ta} . The f magnitudes reveal that both the DB and DT algorithms work better than expected
591 between November and January with f magnitudes of around 80 %. However, for the rest of the
592 year, f remains around a confidence interval of one standard deviation ($f = 68 \%$) for the DT
593 algorithm, while f falls well below this level for several months for the DB, showing that the DT
594 algorithm gives better results than the DB for Camagüey.

595 The Ångström exponents AE_t , AE_a and AE_{ta} do not show good agreement with the spatial
596 and temporal coincident AE_{SP} values when the default-1.5 and the constraint-1.8 values are or are
597 not considered. Those results corroborate the limitation of the MODIS derived AE in general.

598 In the comparison of BAOD vs. AOD_t , AOD_a , AOD_{ta} , the errors are generally of the same
599 order of magnitude as the average values. It is noticeable that the statistics are similar for the sun
600 photometer AOD and the BAOD for the AOD satellite products. This result highlights the potential

601 of BAOD as a reliable source of aerosol information for climatological studies in areas that lack a
602 sun photometer or any other surface measurement.

603 **5. Acknowledgements:**

604 This work has been supported by the Cuban National Program “Meteorology and
605 sustainable development for Cuba” research grant P211LH007-20 and by the Joint Agreement
606 between the University of Valladolid, Spain, and the Cuban Meteorological Institute for aerosol
607 research. JCAM wishes to thank Dr. Loraine Remer and Dr. Andrew Sayer for their contributions
608 to understanding MODIS algorithms. This research has received funding from the European
609 Union’s Horizon 2020 Research and Innovation Program under grant agreement No 654109
610 (ACTRIS-2). We acknowledge the funding provided by MINECO (CTM2015-66742-R) and by
611 the Junta de Castilla y León (VA100U14).

612

613 **6. References:**

- 614 Antuña, J. C., Fonte, A., Estevan, R., Barja, B., Acea, R., Antuña Jr.: J.C., Solar radiation data
615 rescue at Camagüey, Cuba, *Bull. Am. Meteorol. Soc.*, **89**, 1507–1511.
616 <http://dx.doi.org/10.1175/2008BAMS2368.1>, 2008.
- 617 Antuña J. C., Hernández, C., Estevan, R., Barja, B., Fonte, A., Hernández, T., Antuña Jr, J. C.:
618 Camagüey’s solar radiation rescued dataset: preliminary applications, *Óptica Pura y*
619 *Aplicada*, **44** (1), 43-48, 2011.
- 620 Antuña, J. C., Estevan, R., Barja, B.: Demonstrating the Potential for First-Class Research in
621 Underdeveloped Countries: Research on Stratospheric Aerosols and Cirrus Clouds Optical
622 Properties, and Radiative Effects in Cuba (1988–2010), *Bull. Amer. Meteor. Soc.*, **93**,
623 1017–1027. <http://dx.doi.org/10.1175/BAMS-D-11-00149.1>, 2012.
- 624 Antuña-Marrero, J. C., De Frutos Baraja, A., Estevan Arredondo, R.: Joint aerosol research
625 between Cuba and Spain proves fruitful, *EOS*, **97**, doi:10.1029/2016EO060125, 2016.
- 626 Barja, B., Rosas, J., Estevan, R.: Caracterización del contenido integral del vapor de agua
627 atmosférico sobre Cuba obtenido mediante mediciones y modelación, Scientific Report,
628 Grant 200.04070, 77 pp. (In Spanish, unpublished), 2015.
- 629 Bennouna, Y. S., Cachorro, V. E., B., Toledano, C., Berjon, Prats, N., D Fuertes, González, R.;
630 Rodrigo, R., Torres, B., and De Frutos, A. M.: Comparison of atmospheric aerosol
631 climatologies over southwestern Spain derived from AERONET and MODIS. *Remote*
632 *Sens. Environ.* 115, 1272-1284, 2011, doi:10.1016/j.rse.2011.01.011.
- 633 Bennouna, Y. S., Cachorro, V. E., Torres, B., Toledano, C., Berjon, A., de Frutos, A. M. and
634 Alonso Fernandez-Coppel, I.: Atmospheric turbidity determined by the annual cycle of the

635 aerosol optical depth over north-center Spain from ground (AERONET) and satellite
636 (MODIS). *Atmos. Environ.* **67**, 353-364, 2013. doi:10.016./j.atmosenv.2012.10.065.

637 Denjean, C., Formenti, P., Desboeufs, K., Chevaillier, S., Triquet, S., Maillé, M., Cazaunau, M.,
638 Laurent, B., Mayol-Bracero, O.L., Vallejo, P., Quiñones, M., Gutierrez-Molina, I. E.,
639 Cassola, F., Prati, P., and Andrews, E., and Ogren, J. : Size distribution and optical
640 properties of African mineral dust after intercontinental transport, *J. Geophys. Res.*, **121**,
641 7117–7138, doi:10.1002/2016JD024783. 2016.

642 Eck, T., Holben, B., Reid, J. Dubovik, O.: Wavelength dependence of the optical depth of biomass
643 burning, urban, and desert dust aerosols. *J. Geophys. Res.*, **104**, 31333_31349, 1999.

644 Estevan, R.: Certificación de depósito legal facultativo de obras protegidas; software: “Actino
645 2.0”; CENDA 218-2010. (In Spanish), 2010.

646 Estevan R., Antuña, J.C., Barja, B., Hernández, C.E., Hernández, T., García, F., Rosas, J., Platero,
647 I. Y.: Climatología de la Radiación solar en Camagüey 1981 – 2010, *Scientific Report*,
648 Grant 01301216, 41 pp. (In Spanish, unpublished), 2016.

649 Fonte, A., Antuña, J.C.: Caracterización del espesor óptico de banda ancha de los aerosoles
650 troposféricos en Camagüey, Cuba, *Revista Cubana de Meteorología*, **17**, No. 1, pp. 15-26,
651 2011.

652 García, F., Estevan, R., Antuña-Marrero, J. C., Rosas, J., Platero, I. Y., Antuña-Sánchez, J., C.
653 Díaz, N.: Determinación de la Línea Base del Espesor Óptico de Aerosoles de Banda Ancha
654 y comparación con datos de fotómetro solar. *Óptica Pura y Aplicada*, **48**(4), 249-258.doi:
655 10.7149/OPA.48.4.249, 2015.

656 GGO: Manual for the setup and operation of solar radiation instruments. Ed. Guidrometeoizdat,
657 124 pp. (In Russian), 1957.

658 Gkikas, A., Hatzianastassiou, N., Mihalopoulos, N., Katsoulis, V., Kazadzis, S., Pey, J., Querol,
659 X., and Torres, O.: The regime of intense desert dust episodes in the Mediterranean based on
660 contemporary satellite observations and ground measurements, *Atmos. Chem. Phys.*, *13*(23),
661 12135-12154, doi:10.5194/acp-13-12135-2013, 2013.

662 Gkikas, A., Basart, S., Hatzianastassiou, N., Marinou, E., Amiridis, V., Kazadzis, S., Pey, J.,
663 Querol, X., Jorba, O., Gassó, S., and Baldasano, J. M.: Mediterranean desert dust outbreaks
664 and their vertical structure based on remote sensing data, *Atmos. Chem. Phys. Discuss.*, *15*,
665 27675-27748, doi:10.5194/acpd-15-27675-2015, 2015.

666 GOAC: Manual de Observaciones Actinométricas, 37 pp. (*In Spanish, unpublished*), 2010.

667 Gueymard, C.A.: Turbidity determination from broadband irradiance observations: A detailed
668 multicoefficient approach. *J. Appl. Meteorol.* **37**: 414-435, 1998.

669 Gueymard, C. A.: Aerosol turbidity derivation from broadband irradiance observations:
670 Methodological advances and uncertainty analysis. *Solar 2013 Conf.*, Baltimore, MD,
671 American Solar Energy Soc., 8 pp., 2013.

672 Holben, B. N., Tanré, D., Smirnov, A., Eck, T. F., Slutsker, I., Abuhassan, N., Newcomb, W. W.,
673 Schafer, J., Chatenet, B., Lavenue, F., Kaufman, Y. J., Castle, J. V., Setzer, A., Markham,
674 B., Clark, D., Frouin, R., Halthore, R., Karnieli, A., O'Neill, N. T., Pietras, C., Pinker, R.
675 T., Voss, K., Zibordi, G.: An emerging ground-based aerosol climatology: Aerosol optical
676 depth from AERONET, *J. Geophys. Res.*, **106**, 12,067–12,097, 2001.

677 Hsu, N. C., Tsay, S. C., King, M. D., Herman, J. R.: Aerosol Properties Over Bright-Reflecting
678 Source Regions, *IEEE T. Geosci. Remote*, **42**, 557–569, doi:10.1109/TGRS.2004.824067,
679 2004.

680 Hsu, N. C., Tsay, S. C., King, M. D., Herman, J. R.: Deep blue retrievals of Asian aerosol
681 properties during ACE-Asia, *IEEE T. Geosci. Remote*, **44**, 3180–3195,
682 doi:10.1109/TGRS.2006.879540, 2006.

683 Hsu, N. C., Jeong, M.-J., Bettenhausen, C., Sayer, A. M., Hansell, R., Seftor, C. S., Huang, J.,
684 Tsay, S.-C.: Enhanced Deep Blue aerosol retrieval algorithm: the second generation, *J.*
685 *Geophys. Res.*, **118**, 9296–9315, doi:10.1002/jgrd.50712, 2013.

686 IPCC: Climate Change 2013. The Physical Science Basis –Contribution of Working Group I to
687 the Fifth Assessment Report of the Intergovernmental Panel on Climate Change, Stocker
688 TF, Qin D, Plattner G-K, Tignor M, Allen SK, Boschung J, Nauels A, Xia Y, Bex V,
689 Midgley PM. (eds). Cambridge University Press: Cambridge, UK and New York, NY,
690 2013.

691 Kahn, R. A., M. J. Garay, D. L. Nelson, R. C. Levy, M. A. Bull, D. J. Diner, J. V. Martonchik, E.
692 G. Hansen, L. A. Remer, and D. Tanré, Response to “Toward unified satellite climatology
693 of aerosol properties: 3. MODIS versus MISR versus AERONET”, *J. Quant. Spectrosc.*
694 *Radiat. Transfer*, **112**(5), 901–909, doi:10.1016/j.jqsrt.2010.11.001, 2011.

695 Kaufman, Y. J., Wald, A. E., Remer, L. A., Gao, B.-C., Li, R.-R. and Flynn, L.: The MODIS 2.1-
696 μm channel-correlation with visible reflectance for use in remote sensing of aerosol, *IEEE*
697 *T. Geosci. Remote*, **35**, 1286–1298, doi:10.1109/36.628795, 1997a.

698 Kaufman, Y. J., Tanré, D., Remer, L. A., Vermote, E. F., Chu, A., Holben, B. N.: Operational
699 remote sensing of tropospheric aerosol over land from EOS moderate resolution imaging
700 spectroradiometer, *J. Geophys. Res.*, **102**, 17051–17068, doi:10.1029/96JD03988, 1997b.

701 Kaufman, Y. J., Koren, I., Remer, L., Tanré, D., Ginoux, P., and Fan, S.: Dust transport and
702 deposition observed from the Terra-Moderate Resolution Imaging Spectroradiometer
703 (MODIS) spacecraft over the Atlantic Ocean. *J. Geophys. Res. Atmos.*, **110**, D10S12, 2005.

704 Kirilov, T. B., Vlasov, Yu. B., Flaum, M. Ya.: Manual para la operación e instalación de
705 instrumentos de radiación solar, Ed.Guidrometeoizdat, Leningrad, 124 pp. (In Russian),
706 1957.

707 Knippertz, P., Stuut, J.-B.W., 2014. Chapter 1 Introduction. In: Knippertz, P., Stuut, J.-B.W.
708 (Eds.), Mineral Dust: A Key Player in the Earth System. Springer, New York, pp. 1–14,
709 <http://dx.doi.org/10.1007/978-94-017-8978-3>, 2014.

710 Levy, R. C., Remer, L., Mattoo, S., Vermote, E., and Kaufman, Y.: Second-generation operational
711 algorithm: Retrieval of aerosol properties over land from inversion of moderate resolution
712 imaging spectroradiometer spectral reflectance. *J. Geophys. Res. Atmos.*, **112**, D13211,
713 2007.

714 Levy, R. C., Leptoukh, G., Kahn, R., Zubko, V., Gopalan, A., and Remer, L.: A critical look at
715 deriving monthly aerosol optical depth from satellite data. *IEEE Transactions on*
716 *Geoscience and Remote Sensing*, **47**(8), 2942–2956, 2009.

717 Levy, R. C., Remer, L. A., Kleidman, R. G., Mattoo, S., Ichoku, C., Kahn, R., Eck, T. F.: Global
718 evaluation of the Collection 5 MODIS dark-target aerosol products over land, *Atmos.*
719 *Chem. Phys.*, **10**, 10399-10420, doi:10.5194/acp-10-10399-2010, 2010.

720 Levy, R. C., Mattoo, S., Munchak, L. A., Remer, L. A., Sayer, A. M., Patadia, F., Hsu, N. C.: The
721 Collection 6 MODIS aerosol products over land and ocean, *Atmos. Meas. Tech.*, **6**, 2989-
722 3034, doi:10.5194/amt-6-2989-2013, 2013.

723 Levy, R. C., Munchak, L.A., Mattoo, S., Patadia, F., Remer, L.A., and Holz, R. E.: Towards a
724 long-term global aerosol optical depth record: applying a consistent aerosol retrieval
725 algorithm to MODIS and VIIRS-observed reflectance. *Atmos. Meas. Tech.*, **8**, 4083–4110,
726 2015. doi:10.5194/amt-8-4083-2015.

727 Long, C. N., Shi, Y.: The QCRad Value Added Product: Surface Radiation Measurement Quality
728 Control Testing, Including Climatology Configurable Limits, Office of Biological and
729 Environmental Research, U.S. Department of Energy, pp. 69, 2006.

730 Long, C. N., Shi, Y.: An Automated Quality Assessment and Control Algorithm for Surface
731 Radiation Observations. *The Open Atmospheric Science Journal*, **2**, 23-37, 2008.

732 Martínez, E., Campos, A., Borrajero, I., Vázquez, A.: Algunos índices de turbidez del aire en la
733 Ciudad de la Habana, *Revista Cubana de Meteorología*, **1** (1), pp. 57-60, 1988.

734 Mielonen, T., Levy, R. C., Aaltonen, V., Komppula, M., de Leeuw, G., Huttunen, J., Lihavainen,
735 H., Kolmonen, P., Lehtinen, K. E. J., Arola, A.: Evaluating the assumptions of surface
736 reflectance and aerosol type selection within the MODIS aerosol retrieval over land: the
737 problem of dust type selection, *Atmos. Meas. Tech.*, **4**, 201–214, doi:10.5194/amt-4-201-
738 2011, 2011.

739 Mishchenko M.I., Li Liu, Geogdzhayev, I. V., Travis, L. D., Cairns, B., Lacis, A. A.: Toward
740 unified satellite climatology of aerosol properties.: 3. MODIS versus MISR versus
741 AERONET, *J. Quant. Spectrosc. Radiat. Transfer*, **111**, 540-552, 2010.

742 Ohmura, A., Dutton, E., Forgan, B., Froehlich, C., Gilgen, H., Hegner, H., Heimo, A., Koenig-
743 Langlo, G., McArthur, B., Mueller, G., Philipona, R., Pinker, R., Whitlock, C., Wild, M.:
744 Baseline Surface Radiation Network (BSRN/WCRP), a new precision radiometry for
745 climate research. *Bull. Am. Meteorol. Soc.*, **79**, 2115-2136, 1998.

746 Papadimas, C.D., Hatzianastassiou, N., Mihalopoulos, N., Kanakidou, M., Katsoulis, B. D., and
747 Vardavas, I.: Assessment of the MODIS Collections C005 and C004 aerosol optical depth
748 products over the Mediterranean basin, *Atmos. Chem. Phys.*, **9**, 2987-2999;
749 doi.org/10.5194/acp-9-2987-2009, 2009.

750 Prospero, J. M., Lamb, P. J.: African droughts and dust transport to the Caribbean: Climate change
751 implications. *Science*, **302**, 1024–1027, 2003.

752 Prospero, J. M., Mayol-Bracero, O. L.: Understanding the transport and impact of African dust on
753 the Caribbean Basin, *Bull. Am. Meteorol. Soc.*, **94**(9), 1329–1335, 2013.

754 Prospero, J. M., Collard, F.-X., Molinié, J., Jeannot, A.: Characterizing the annual cycle of African
755 dust transport to the Caribbean Basin and South America and its impact on the environment
756 and air quality, *Global Biogeochem. Cycles*, **29**, 757–773, doi:10.1002/2013GB004802,
757 2014.

758 Remer, L. A., Tanré, D., Kaufman, Y. J., Ichoku, C., Mattoo, S., Levy, R., Chu, D. A., Holben, B.
759 N., Dubovik, O., Smirnov, A., Martins, J.V., Li, R. R., Ahmad, Z.: Validation of MODIS
760 aerosol retrieval over ocean. *Geophys. Res. Lett.*, 29(12), 1618, 2002.

761 Remer, L. A., Kaufman, Y. J., Tanre, D., Mattoo, S., Chu, D. A., Martins, J. V., Li, R. R., Ichoku,
762 C., Levy, R. C., Kleidman, R. G., Eck, T.F., Vermote, E., Holben, B. N.: The MODIS
763 aerosol algorithm, products, and validation". *J. Atmos. Sci.*, 62(4), 947-973, 2005.

764 Remer, L. A., Tanré, D., Kaufman, Y., Levy, R., and Mattoo, S.: Algorithm for remote sensing of
765 tropospheric aerosol from MODIS: Collection 005. [https://modis-](https://modis-images.gsfc.nasa.gov/docs/MOD04:MYD04_ATBD_C005_rev1.pdf)
766 [images.gsfc.nasa.gov/docs/MOD04:MYD04_ATBD_C005_rev1.pdf](https://modis-images.gsfc.nasa.gov/docs/MOD04:MYD04_ATBD_C005_rev1.pdf).

767 Sayer, A. M., Hsu, N. C., Bettenhausen, C., Jeong, M.-J.: Validation and uncertainty estimates for
768 MODIS Collection 6 “Deep Blue” aerosol data, *J. Geophys. Res. Atmos.*, **118**, 7864–7872,
769 doi:10.1002/jgrd.50600, 2013.

770 Sayer, A. M., Munchak, L. A., Hsu, N. C., Levy, R. C., Bettenhausen, C., Jeong, M.-J.: MODIS
771 Collection 6 aerosol products: Comparison between Aqua’s e-Deep Blue, Dark Target, and

772 “merged” data sets, and usage recommendations, *J. Geophys. Res. Atmos.*, **119**, 13,965–
773 13,989, doi:10.1002/2014JD022453, 2014.

774 Santese, M., De Tomasi, M. F. and, Perrone, M. R.: AERONET versus MODIS aerosol parameter
775 at different spatial resolutions over southeast Italy, *J. Geophys. Res.*, **112**, D10214,
776 doi:10.1029/2006JD007742, 2007.

777 Seinfeld, J. H. and S. N. Pandis.: Atmospheric chemistry and physics: from air pollution to climate
778 change. 3rd edition, John Wiley & Sons, Inc., ISBN: 9781118947401, 1120 pp., 2016.

779 Smirnov, A., Holben, B. N., Eck, T. F., Dubovik, O., Slutsker, I.: Cloud-screening and quality
780 control algorithms for the AERONET database, *Remote Sens. Environ.*, **73**(3), 337–349,
781 2000.

782 Swap, R., Garstang, M., Greco, S., Talbot, R., Kallberg, P.: Saharan dust in the Amazon basin.
783 *Tellus*, **44B**, 133–149, 1992.

784 Tanré, D., Kaufman, Y. J., Herman, M., Mattoo, S.: Remote sensing of aerosol properties over
785 oceans using the MODIS/EOS spectral radiances, *J. Geophys. Res.*, **102**, 16971–16988,
786 1997.

787 Velasco-Merino, C., Mateos, D., Toledano, C.; Prospero, J. M., Molinie, J., Euphrasie-Clotilde,
788 L., González, R., Cachorro, V. e., Calle, A., and De Frutos, A. M.: Impact of long-range
789 transport over the Atlantic Ocean on Saharan dust optical and microphysical properties.
790 *Atmos. Chem. Phys. Disc.*, <https://doi.org/10.5194/acp-2017-1089>, 2017

791 Wagner, F., and Silva A. M.: Some considerations about Ångström exponent distributions. *Atmos.*
792 *Chem. Phys.*, **8**, 481–489, 2008.

793 Witte, J. C., A.R. Douglass, A. da Silva, O. Torres, R.C. Levy, and B.N. Duncan, (2011). NASA
794 A-Train and Terra observations of the 2010 Russian wildfires, *Atmos. Chem. Phys.*, 11,
795 9287-9301, doi:10.5194/acp-11-9287-2011, 2011.

796 Yu, H. , M. Chin, T. Yuan, H. Bian, L. A. Remer, J. M. Prospero, A. Omar, D. Winker, Y. Yang,
797 Y. Zhang, Z. Zhang and C. Zhao, The fertilizing role of African dust in the Amazon
798 rainforest: A first multiyear assessment based on data from Cloud-Aerosol Lidar and
799 Infrared Pathfinder Satellite Observations, *Geophys. Res. Lett.*, **42**, 1984–1991,
800 doi:10.1002/2015GL063040, 2015.

801 Zhao, T. X.-P., Stowe, L. L., Smirnov, A., Crosby, D., Sapper, J., McClain, C. R.: Development
802 of a global validation package for satellite oceanic aerosol optical thickness retrieval based
803 on AERONET observations and its application to NOAA/NESDIS operational aerosol
804 retrievals, *J. Atmos. Sci.*, **59**, 294– 312, 2002.

805
806
807
808
809
810
811
812
813
814
815
816
817
818

819 **Tables:**

820

821 Table 1: Aerosol products from the MODIS Collection 6 dataset used in the present study

Product	Description
Deep_Blue_Aerosol_Optical_Depth_550_Land_Best_Estimate	Deep Blue AOT at 0.55 micron for land with higher quality data (Quality flag=2,3)
Deep_Blue_Angstrom_Exponent_Land	Deep Blue Angstrom Exponent for land with all quality data (Quality flag=1,2,3)
Optical_Depth_Land_And_Ocean	AOT at 0.55 micron for both ocean (Average) (Quality flag=1,2,3) and land (corrected) (Quality flag=3)

822

823

824 Table 2: Information about Cuban actinometrical stations operating under the Solar Radiation Diagnostic Service

825 (SRDS). Available number of BAOD observations included in column 6 and the period covered in the last column.

Code	Station Name	Latitude	Longitude	Height (m)	No. Obs.	Period
78355	Camagüey (CMW)	21.42	-77.85	122 m	2495	2001-2015
78330	Jovellanos (JVN)	22.80	-81.14	23 m	1182	2010-2015
78342	Topes de Collantes (TPC)	21.92	-80.02	766 m	1358	2011-2015
78321	Santa Fé (LFE)	21.73	-82.77	32 m	1756	2011-2015

826

827

828 Table 3: Number of available non-negative AOD_a, AOD_t, AE_a and AE_t data spatially coincident with the Camagüey

829 sunphotometer in a radius of 25 km for each retrieval algorithm, DB and DT for the whole period 2001-2015, as well

830 as the period 2008-2014, when sunphotometer data, AOD_{SP} and AE_{SP}, are available.

831

832

Period	2001-2015			2008-2014		
Algorithm	DB		DT	DB		DT
Parameter	AOD	AE	AOD	AOD	AE	AOD
Terra	6884	8111	6311	3418	4024	3166
Aqua	2445	3909	2869	1329	1534	2093

835

836

837

838 Table 4: Statistics of the comparison between collocated daily means of AOD_t and AOD_a with AOD_{SP} and the
 839 combined AOD_{ta} .

	AOD_{SP} vs. AOD_t		AOD_{SP} vs. AOD_a		AOD_{SP} vs. AOD_{ta}	
	DB	DT	DB	DT	DB	DT
RMSE	0.084	0.060	0.065	0.062	0.078	0.061
MAE	0.062	0.045	0.046	0.047	0.056	0.046
BIAS	-0.053	-0.001	-0.033	0.006	-0.046	0.002
R	0.730	0.729	0.785	0.779	0.741	0.753
f	0.656	0.803	0.763	0.795	0.694	0.800
Cases	311	335	169	254	480	589

840

841

842 Table 5: Statistics of the comparison between collocated single observation of AOD_t and AOD_a with AOD_{SP} and
 843 combined AOD_{ta} .

	AOD_{SP} vs. AOD_t		AOD_{SP} vs. AOD_a		AOD_{SP} vs. AOD_{ta}	
	DB	DT	DB	DT	DB	DT
RMSE	0.081	0.061	0.063	0.064	0.076	0.062
MAE	0.059	0.046	0.044	0.050	0.054	0.047
BIAS	-0.048	0.007	-0.027	0.017	-0.042	0.010
R	0.716	0.701	0.817	0.794	0.744	0.742
f	0.664	0.773	0.773	0.784	0.699	0.777
Cases	880	900	419	500	1299	1400

844

845

846 Table 6: Statistics of the comparison between AE_t , AE_a and AE_{ta} with AE_{SP} for single observations and daily mean
 847 values.

	Single observations			Single observations (Except AE 1.5 & 1.8)			Collocated daily means			Collocated daily means (Except AE 1.5 & 1.8)		
	AE_t	AE_a	AE_{ta}	AE_t	AE_a	AE_{ta}	AE_t	AE_a	AE_{ta}	AE_t	AE_a	AE_{ta}
RMSE	0.637	0.692	0.658	0.575	0.609	0.587	0.637	0.659	0.645	0.548	0.578	0.561
MAE	0.494	0.553	0.516	0.446	0.496	0.464	0.490	0.512	0.498	0.431	0.466	0.445
BIAS	-0.327	-0.337	-0.331	-0.129	-0.101	-0.119	-0.398	-0.384	-0.393	-0.189	-0.139	-0.167
R	-0.187	-0.426	-0.272	-0.191	-0.444	-0.269	-0.259	-0.414	-0.308	-0.124	-0.400	-0.236
Cases	615	374	989	353	189	542	311	169	480	172	120	292

848

849

850 Table 7: Number of coincident cases of AOD_t, AOD_a, AOD_{ta} with BAOD both for the DB and for DT algorithms.

Station:	BAOD vs. AOD _t		BAOD vs. AOD _a		BAOD vs. AOD _{ta}	
	DB	DT	DB	DT	DB	DT
Camagüey	166	171	66	79	232	250
Topes de Collantes	112	138	49	76	161	214
Jovellanos	65	65	35	34	100	99
La Fe	34	66	46	85	80	151
All combined	377	440	196	274	573	714

851

852 Table 8: Statistics of the comparison between the single observations of BAOD at the four actinometrical stations
 853 coincident in space and time with the single observation (L2) of AOD_t, AOD_a and AOD_{ta}. In bold, the values of best
 854 agreement.

Camagüey, La Fe, Topes de Collantes & Jovellanos						
	BAOD vs. AOD _t		BAOD vs. AOD _a		BAOD vs. AOD _{ta}	
	DB	DT	DB	DT	DB	DT
RMSE	0.080	0.087	0.073	0.088	0.078	0.088
MAE	0.055	0.063	0.048	0.066	0.052	0.064
BIAS	0.001	0.027	0.014	0.049	0.005	0.035
R	0.455	0.325	0.501	0.417	0.468	0.355
Cases	373	436	191	268	564	704

855

856

857

858

859

860

861

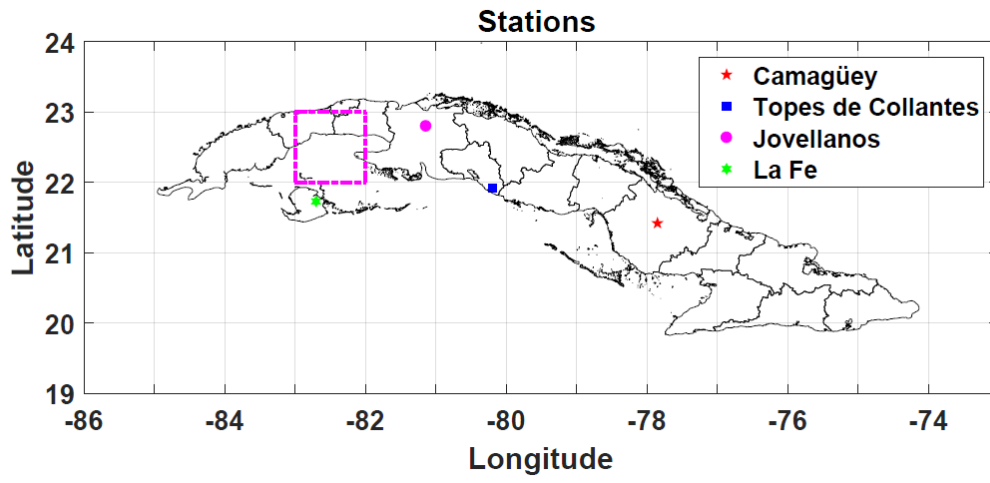
862

863

864

865 **Figure and Captions:**

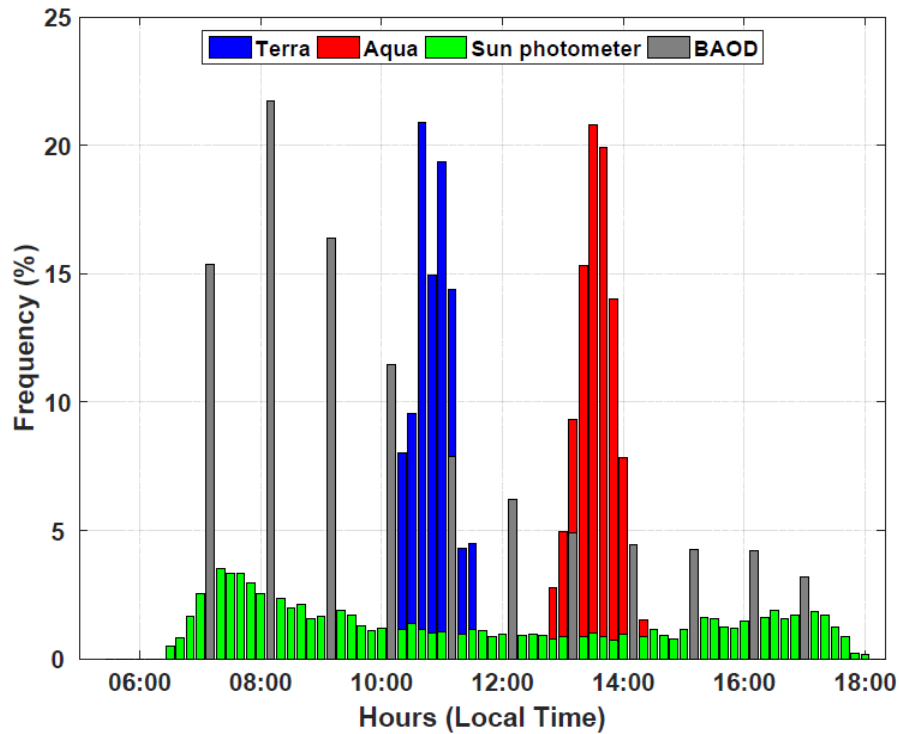
866



867

868 **Figure 1:** Map of Cuba locating the stations where the sun photometer and the four broadband
869 pyr heliometer observations are conducted.

870

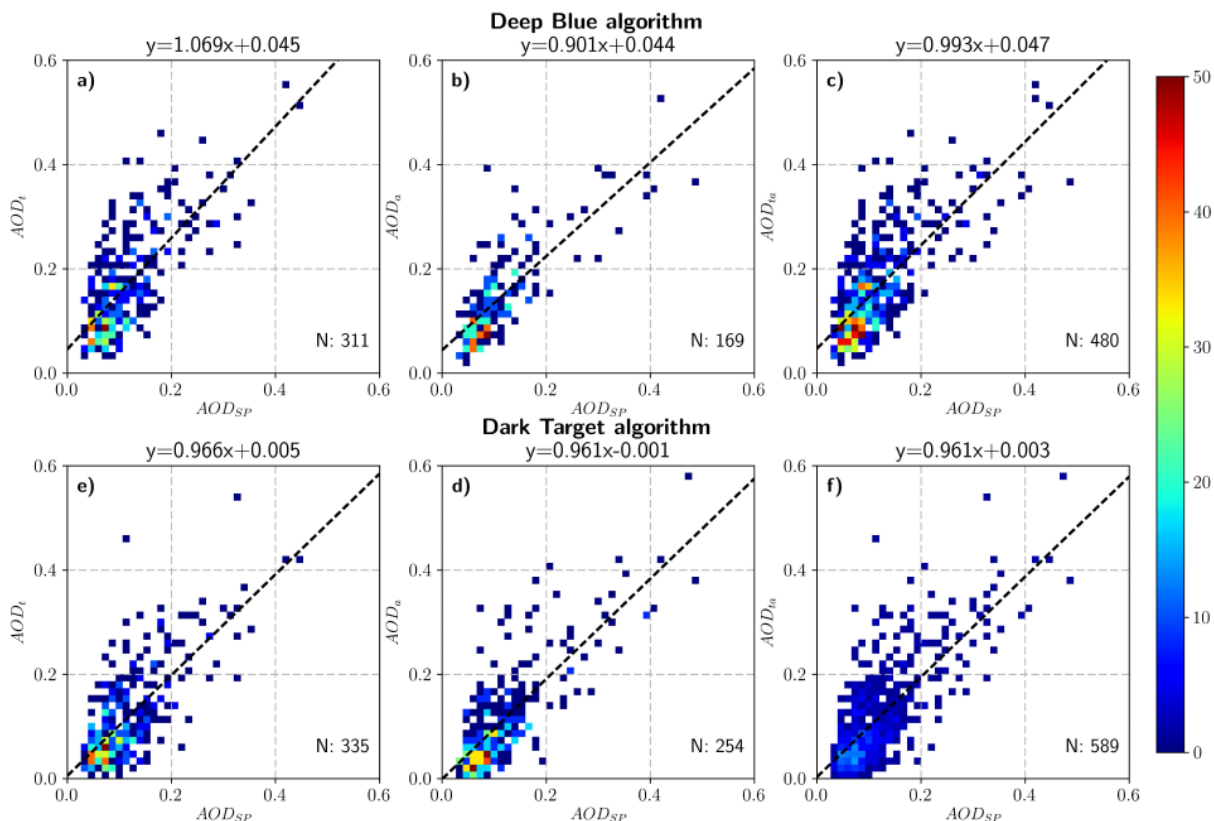


872

873 **Figure 2:** Frequencies of the time of the day (Local Time) overpass of Terra and Aqua (blue and
 874 red respectively) Camagüey's sun photometer site in a radius of 25 km for the period
 875 2001 to 2015. In green the time frequencies for the Camagüey's sun photometer
 876 observations in the period 2008 to 2014. In addition, the time frequencies for the direct
 877 radiation observations used to calculate the BAOD. The bar width is 10 minutes for
 878 Terra, Aqua and the sun photometer and 1 hour for the BAOD.

879

880

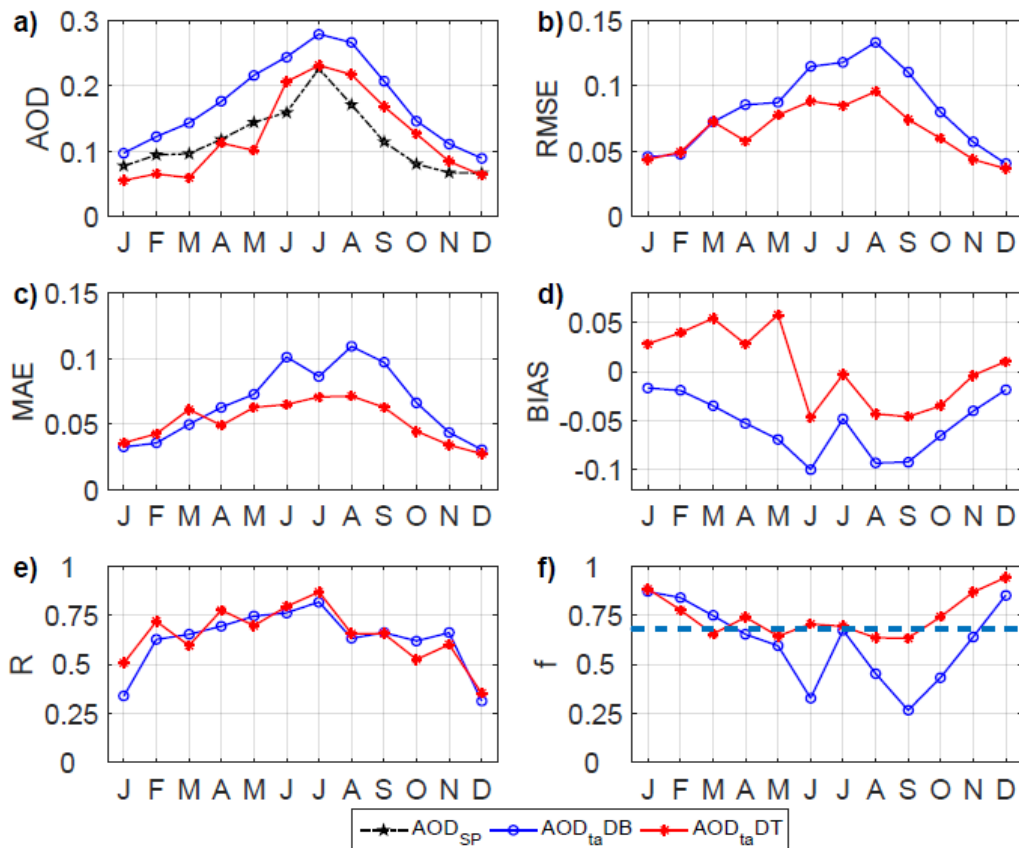


881

882 **Figure 3:** Collocated “daily mean” density scatter plots of the coincident AOD observations from
883 the sun photometer and Terra and Aqua MODIS instruments for DB and DT
884 algorithms.: a) to c) AOD_{SP} vs AOD_t , AOD_a and AOD_{ta} respectively for DB
885 algorithm; d) to f) Idem for DT algorithm. The data density is represented by the color
886 scale, showing the number of data points located in a particular area of the plot. Linear
887 regression is given by the black discontinuous line and the corresponding equation.
888 The number of data points appears in the right bottom.

889

890



892

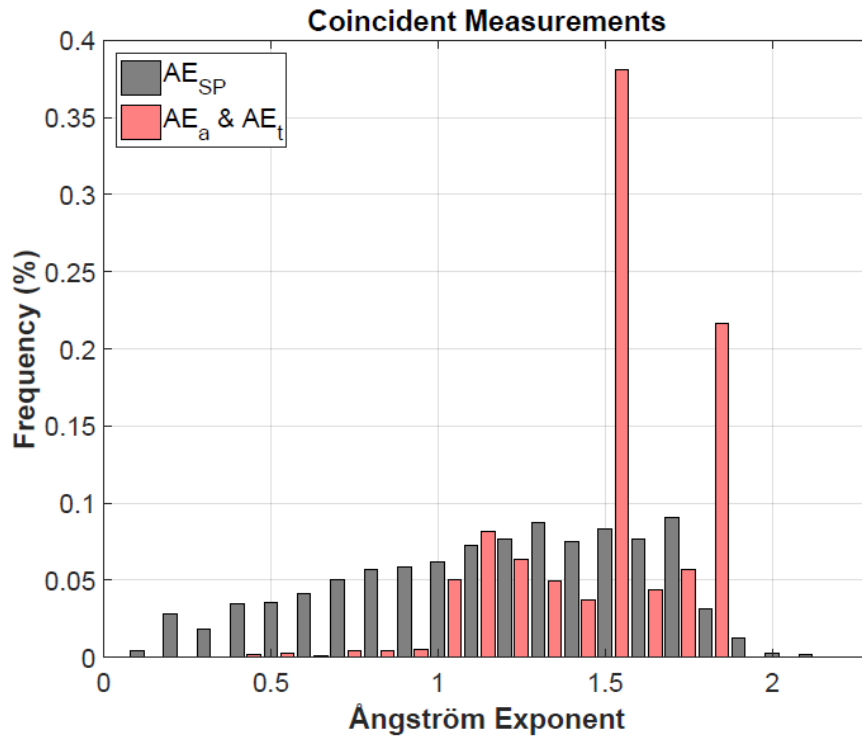
893 **Figure 4:** Monthly means and statistics (RMSE, MAE.....) resulting from the comparison
 894 between AOD_{SP} and AOD_{ta} for both DB and DT algorithms: a) Monthly means of the
 895 AOD_{SP} and AOD_{ta} for both DB and DT algorithms; b) RMSE for the comparison
 896 between AOD_{SP} and AOD_{ta} for both DB and DT algorithms; c) Idem for MAE, d) for
 897 BIAS, e) for R and f) for f. The blue discontinuous line at f= 68 % represent one
 898 standard deviation confidence interval for the EE indicator.

899

900

901

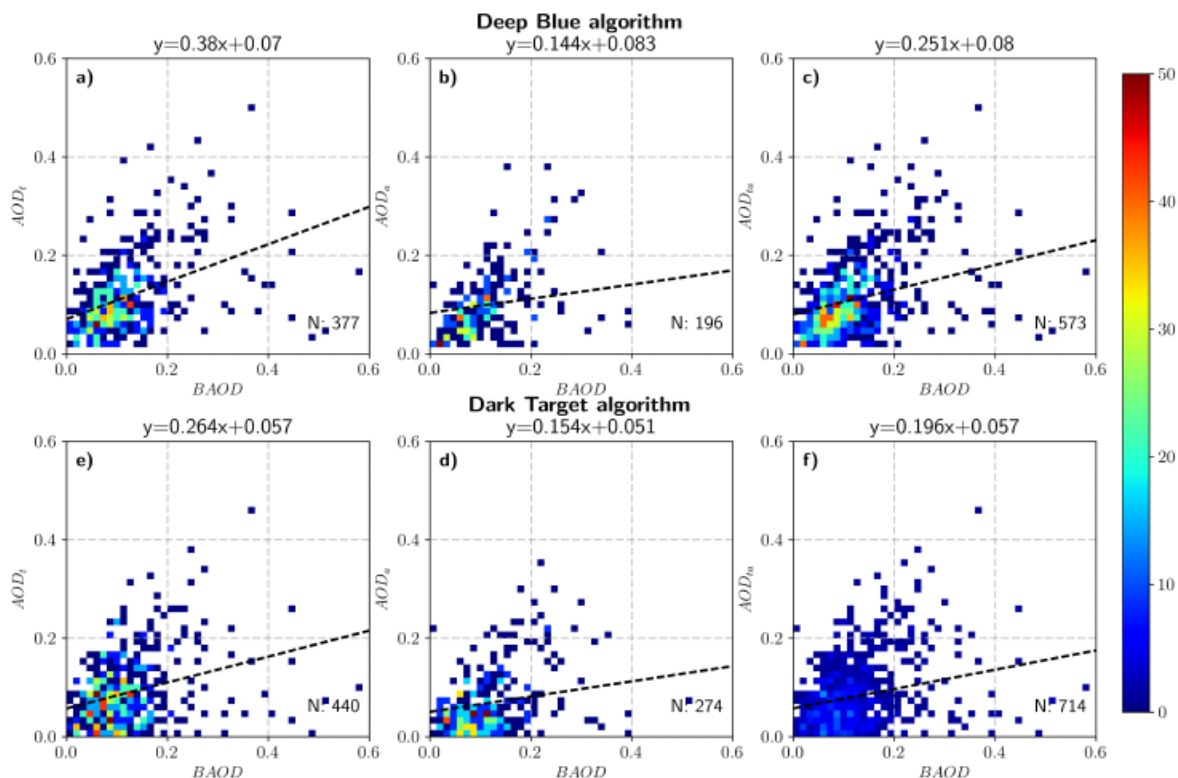
902



904

905 **Figure 5:** Frequency distribution of the Angstrom exponent (AE) values from both MODIS
 906 instruments Terra and Aqua and the sun photometer coincident in ± 30 minutes and 25
 907 km radius around Camagüey.

908



910

911 **Figure 6:** Single observations density scatter plots of the coincident BAOD observations from the

912 broadband pyrheliometer and Terra and Aqua MODIS instruments for DB and DT

913 algorithms.: a) to c) BAOD vs. AOD_t , AOD_a and AOD_{ta} respectively for DB

914 algorithm; d) to f) Idem for DT algorithm. The data density is represented by the color

915 scale, showing the number of data points located in a particular area of the plot.

916 Linear regression line is shown by the black discontinuous line and the corresponding

917 equation. The number of data points appears in the right bottom.

918

919